GPS Solutions (2025) 29:142
https://doi.org/10.1007/s10291-025-01897-7

RESEARCH

Visual RTK positioning enhanced by pole motion constraint

Xiaoji Niu[1,2] · **Jiahao Ai**[1,3] · **Qijin Chen**[1]

Received: 10 January 2025 / Accepted: 1 June 2025
© The Author(s), under exclusive licence to Springer-Verlag GmbH Germany, part of Springer Nature 2025

Abstract

High-precision point positioning measurement has a wide range of applications in smart city construction. Global navigation satellite system real-time kinematic (RTK) technology is an important means for high-precision point positioning measurement. It is widely used in surveying projects such as engineering control measurement, topographic surveying, cadastral mapping, and construction staking. To expand the application scenarios and enhance the surveying functions, researchers have developed products like tilt RTK and visual RTK. However, current visual RTK products are still in an immature stage although products have been launched. Most visual RTK products require users to manually hold the surveying pole and walk a certain distance to form the photogrammetry baseline. During this process, users must keep the camera aimed at the target points from different angles. This manual operation is tedious and often leads to unreliable and inconsistent surveying results. Furthermore, the factors influencing the surveying accuracy have not been investigated in a quantitative way. To address these issues, this paper proposes a visual RTK positioning method without the handheld walking operation, instead relies on swinging the surveying pole with its tip in contact with the ground. It realizes high-precision photogrammetry through fully utilizing fix-point rigid body rotation constraints in such swing mode, and is named as inertial photogrammetry RTK pole. We conducted a detailed analysis and comparison of photogrammetry accuracy between this swinging mode and the traditional handheld walking mode. Field test results show that the proposed swinging mode (with only 1.5–2 m baseline) achieves an accuracy comparable to the handheld walking mode with over 8 m baseline, when surveying target points 15 m away. The surveying root mean squared error can approximately reach 6 cm for target points at 15 m, 4 cm for target points at 10 m, and 2 cm for target points at 6 m. The results prove that the proposed method is an accuracy-competitive, time-saving, operation-convenient, and application-friendly approach that can effectively improve current visual RTK.

Keywords Visual RTK · Photogrammetry · GNSS/INS Integrated navigation · Fix-point rigid body rotation

Introduction

Global navigation satellite system (GNSS) real-time kinematic (RTK) achieves positioning with centimeter-level accuracy in kinematic mode and is widely applied in fields such as navigation, positioning, and digital mapping (Teunissen and Montenbruck 2017; Liu et al. 2020). A typical RTK setup involves fixing the GNSS antenna and receiver on a mounting pole (Gučević et al. 2024). During the measurement process, the pole must be leveled with a circular bubble to maintain vertical alignment (Lin 2021). The RTK positioning result is calculated from the phase center of the antenna to the pole tip, thus obtaining the coordinates of the target point on the ground, as shown in Fig. 1a. However, the classical RTK has the following shortcomings in terms of measurement efficiency and applicability:

- GNSS signal is frequently disturbed and blocked by trees, buildings and other facilities, resulting in the degradation of positioning accuracy and even unavailability (Teunissen and Montenbruck 2017).
- RTK measurements require the surveying pole to be adjusted and held vertically, which limits the measurement efficieny(Li and Chen 2019).

✉ Qijin Chen
chenqijin@whu.edu.cn

[1] GNSS Research Center, Wuhan University, Wuhan, China

[2] Artificial Intelligence Institute, Wuhan University, Wuhan, China

[3] School of Geodesy and Geomatics, Wuhan University, Wuhan, China

Published online: 16 June 2025

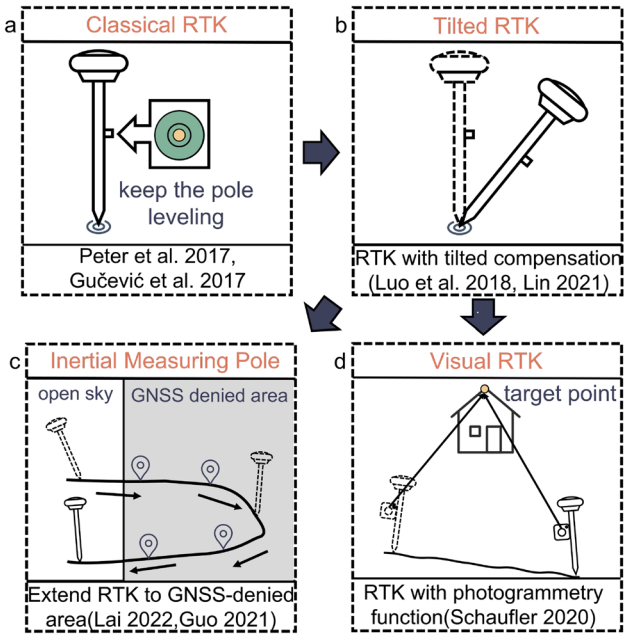

Fig. 1 Three improvements of classical RTK

- RTK measurements become unusable when the target points are located in difficult locations such as corners, steep slopes, or underneath vehicles (Deng et al. 2022).

To address these issues, researchers have proposed improvements to RTK surveying methods and equipment functionalities, including RTK with tilt compensation function (Tilt RTK) (Luo et al. 2018; Lin 2021), surveying pole with inertial dead reckoning capabilities (Inertial positioning pole) (Lai 2022; Guo 2021), and RTK with photogrammetry function (Visual RTK) (Schaufler et al. 2020), as illustrated in Fig. 1.

Tilt RTK (Fig. 1b): Tilt RTK uses attitude sensors such as IMU (Inertial Measurement Units) and magnetometer to calculate the attitude angles of the surveying pole in real time, allowing the GNSS antenna phase center position to be compensated to the tip of the pole (the target point) (Li and Chen 2019; Mark and Nicholas 1996; Bruno 2009). Tilt RTK eliminates the need for pole leveling and can measure target points inaccessible to classical RTK, such as control points at building corners or beneath vehicles. This makes the measurement process more convenient and extends RTK positioning to constrained environments (Luo et al. 2018). With the development of tilt RTK technology, researchers applied integrated navigation technology to tilt RTK, further improving its performance. Wang et al. (2025) proposed a lever arm error estimation method by leveraging GNSS/INS integration. Lin (2021) employed lever-arm compensated zero-velocity update (LA-ZUPT) to effectively constrain the position error divergence and reduce the defects of the tilt angle.

Inertial positioning pole (Fig. 1c): Although tilt RTK extends the range of RTK applications, it still suffers the limitations in GNSS-denied areas. Lai (2022); Guo (2021) proposed a method for inertial positioning pole, which extends the RTK positioning capability to some extent into satellite-denied areas. The core idea is to use the pole as a walking stick with the pole tip periodically landing on the ground, which allows the inertial navigation system (INS) to utilize flexible LA-ZUPT. The inertial positioning pole effectively extends the measurement capabilities and application scope of RTK. Its experimental results show that the inertial positioning pole can achieve positioning accuracy better than 0.2%D (D denotes the travel distance within the GNSS-denied area), with measurement accuracy still better than 0.1 m at a distance of 100 m (Lai et al. 2023).

The classical RTK, tilt RTK, and inertial positioning pole are all contact-based positioning devices, which require physical contact the tip of the RTK pole on the target point for accurate surveying. However, in many practical applications, certain target points may be inaccessible due to terrain or environmental factors (such as water bodies, marshes, or hazardous/polluted areas), preventing direct contact with the target point.Photogrammetry, renowned for its large-scale coverage and high efficiency, is a widely adopted non-contact measurement technique in the fields of surveying and geographic information. With the advancement of GNSS technology, GNSS-aided photogrammetry has emerged and has been extensively researched and applied in UAV (unmanned aerial vehicle) aerial photogrammetry. However, the combined measurement method of GNSS and photogrammetry is rarely used on measuring poles(Colomina and Molina 2014; Štroner et al. 2020, 2021). Schaufler et al. (2020) proposed a photogrammetry solution using GNSS/INS to provide absolute pose (position and attitude) assistance, which verified the feasibility of using RTK surveying pole for non-contact measurement. Knut (2020) proposed an invention which describes a camera module attached on a pole with a GNSS-antenna, computing the 3D-coordinates of surrounding target points by forward intersection using a series of images. Guo et al. (2020) proposes a monocular vision coordinate transfer method with IMU aiding. This method solves the rotation matrix between the camera and the geographic coordinate system through IMU, and then obtains the three-dimensional coordinates of the points to be measured. In 2020, Leica Geosystems launched the visual RTK product GS18. The device integrates a mono-camera on the basis of GNSS/INS system, and estimates the 3D position and attitude through integrated navigation system. The position and attitude estimation results of GNSS/INS are fed into the photogrammetry algorithm to measure some inaccessible target points, which makes the point

measurement of RTK expand from contact measurement to non-contact measurement. GS18 has a measurement accuracy of 5 cm for the target points 2–10 m away from the surveying pole (Schaufler et al. 2020). Peppa et al. (2024) further evaluated the photogrammetric accuracy of Leica GS18 through field experiments. The study involved moving slowly along a wall, maintaining a distance of 4–5 ms, while capturing photographs to observe the target points on the wall. The results revealed that the photogrammetry RTK achieved a 3D RMSE of approximately 3.5 cm. Similar to the GS18, there are other visual RTK products such as i93 from CHC Navigation and vRTK2 from Hi-Target (Wu et al. 2024), which follow the same principle.

Currently, most visual RTK products on the market form a photogrammetric baseline by walking a certain distance while holding the surveying pole to complete the photogrammetry (Fig. 1d). This measurement method requires maintaining intervisibility between the target points and the camera during the whole process, and sufficient space is needed to ensure the walking distance (photogrammetric baseline) for measurement accuracy. However, this method has limitations in practical scenarios. When there are many obstacles in the operation area (as shown in Fig. 2), or when the space is narrow and free movement is difficult, the line-of-sight between the visual RTK and the target point may be blocked, resulting in a failure to position. Additionally, current visual RTK only provides the actual statistical accuracy of the equipment, and parameters closely related to measurement accuracy, such as the distance between the target point and the camera, and the walking distance to form the photogrammetric baseline, have not been studied in public literature. Therefore, aiming at the above issues of current visual RTK, this paper proposes a visual RTK positioning method without holding and walking. It forms the photogrammetric baseline by swinging the surveying pole with its tip contact on the ground at a fixed point, and further benefit from additional motion constraints (inertial photogrammetry RTK pole). The main contributions of this paper are as follows: (1) A new photogrammetry algorithm is proposed that allows for remote point measurement by swinging the pole at a fixed point, without walking a certain distance to form a sufficiently long baseline for point measurement, which improves the feasibility and efficiency of visual RTK operations. (2) The quantitative relation between major influencing factors (e.g. the baseline length of photogrammetry and the target point distance) and surveying accuracy is studied through simulations and real tests. The positioning error of the proposed visual RTK is quantitatively analyzed and validated through real test measurements, enabling an effective assessment of its superior surveying performance.

Methodology

Overview

The general idea of the inertial photogrammetry RTK pole to approach photogrammetry is to use the IMU mounted on the surveying pole to provide high-precision pose for the camera, and then use the image series captured by the camera from different viewpoints for forward intersection to achieve non-contact measurement. The hardware design is shown in Fig. 3: a GNSS antenna is mounted at the top of the pole, the camera and IMU are rigidly installed in the middle of the pole. During photogrammetry, the pole is first swung under the open sky to complete the initialization (Chen et al. 2020; Lai 2022), and then the camera is kept observing the target points, swinging the surveying pole at a fixed point to form a photogrammetric baseline and complete the photogrammetry.

The process of the inertial photogrammetry RTK pole algorithm is shown in Fig. 4. The overall algorithm is divided into two main modules: the inertial positioning pole algorithm and the photogrammetry algorithm. In the inertial positioning pole algorithm module, in addition to GNSS position correction, the rigid body rotation motion provides zero-velocity update (ZUPT) and GNSS heading correction opportunities for INS, which further suppresses INS error

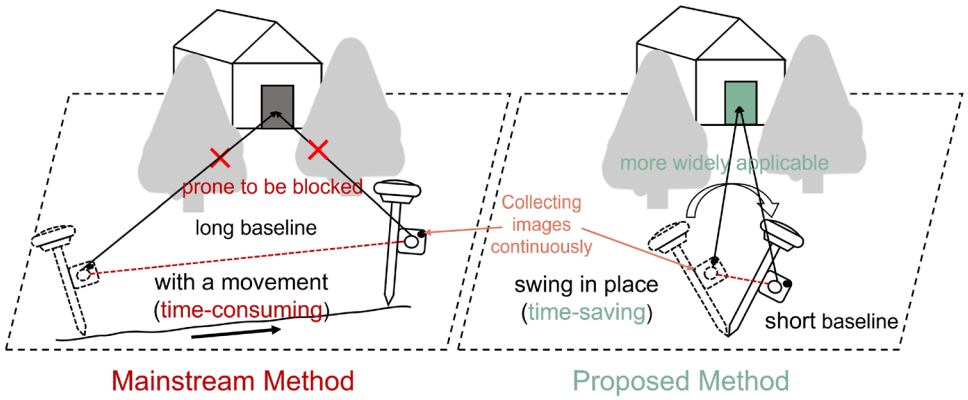

Fig. 2 Comparison between mainstream visual RTK measurement method and the proposed method

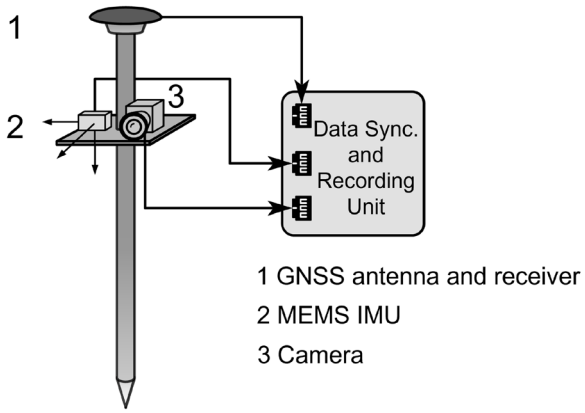

Fig. 3 Hardware design of the inertial photogrammetry RTK pole

divergence and provides high-precision pose for subsequent photogrammetry.

System model

In order to solve the nonlinearity problem of the system, the GNSS/INS loosely-coupled system chooses the extended Kalman filter (EKF) for the integrated navigation solution, and the state vector of the filter consists of the 9-dimensional navigation state error and the 12-dimensional IMU sensor error:

$$\delta\mathbf{x}(\mathrm{t}) = \left[(\delta\mathbf{r}^{\mathrm{n}})^{\mathrm{T}} \ (\delta\mathbf{v}^{\mathrm{n}})^{\mathrm{T}} \ \boldsymbol{\phi}^{\mathrm{T}} \ \mathbf{b}_{\mathrm{g}}^{\mathrm{T}} \ \mathbf{b}_{\mathrm{a}}^{\mathrm{T}} \ \mathbf{s}_{\mathrm{g}}^{\mathrm{T}} \ \mathbf{s}_{\mathrm{a}}^{\mathrm{T}} \right]^{\mathrm{T}} \tag{1}$$

Navigation state errors include position error $\delta\mathbf{r}^{\mathrm{n}}$, speed error $\delta\mathbf{v}^{\mathrm{n}}$, and attitude error $\boldsymbol{\phi}$; IMU sensor errors include gyroscope and accelerometer bias error $\mathbf{b}_{\mathrm{g}}$, $\mathbf{b}_{\mathrm{a}}$, gyroscope and accelerometer scale factor error $\mathbf{s}_{\mathrm{g}}$, $\mathbf{s}_{\mathrm{a}}$.

The continuous time differential equation of the system is

$$\delta\dot{\mathbf{x}}(\mathrm{t}) = \mathbf{F}(\mathrm{t})\delta\mathbf{x}(\mathrm{t}) + \mathbf{G}(\mathrm{t})\mathbf{w}(t) \tag{2}$$

$\mathbf{F}(\mathrm{t})$ is a system matrix obtained by differentiating the components in $\mathbf{x}(\mathrm{t})$. The differential equations for position, velocity, and attitude are as follows:

$$\begin{aligned}
\delta\dot{\mathbf{r}}^{\mathrm{n}} &= -\boldsymbol{\omega}_{\mathrm{en}}^{\mathrm{n}} \times \delta\mathbf{r}^{\mathrm{n}} + \delta\boldsymbol{\theta} \times \mathbf{v}^{\mathrm{n}} + \delta\mathbf{v}^{\mathrm{n}} \\
\delta\dot{\mathbf{v}}^{\mathrm{n}} &= \mathbf{C}_b^{\mathrm{n}}\delta\mathbf{f}^{\mathrm{b}} + \mathbf{f}^{\mathrm{n}} \times \boldsymbol{\phi} - \left(2\boldsymbol{\omega}_{\mathrm{ie}}^{\mathrm{n}} + \boldsymbol{\omega}_{\mathrm{en}}^{\mathrm{n}}\right) \times \delta\mathbf{v}^{\mathrm{n}} \\
&\quad + \mathbf{v}^{\mathrm{n}} \times \left(2\delta\boldsymbol{\omega}_{\mathrm{ie}}^{\mathrm{n}} + \delta\boldsymbol{\omega}_{\mathrm{en}}^{\mathrm{n}}\right) + \delta\mathbf{g}_{\mathrm{p}}^{\mathrm{n}} \\
\dot{\boldsymbol{\phi}} &= -\boldsymbol{\omega}_{\mathrm{in}}^{\mathrm{n}} \times \boldsymbol{\phi} + \delta\boldsymbol{\omega}_{\mathrm{in}}^{\mathrm{n}} - \delta\boldsymbol{\omega}_{\mathrm{ib}}^{\mathrm{n}}
\end{aligned} \tag{3}$$

The gyroscope and accelerometer zero bias and scale factor errors are modeled as first-order Gaussian Markov processes:

$$\begin{cases}
\dot{\mathbf{b}}_{\mathrm{g(t)}} = -\dfrac{1}{\mathrm{T}_{\mathrm{gb}}}\mathbf{b}_{\mathrm{g(t)}} + \mathbf{w}_{\mathrm{gb}}(\mathrm{t}) \\
[10pt]\dot{\mathbf{b}}_{\mathrm{a(t)}} = -\dfrac{1}{\mathrm{T}_{\mathrm{ab}}}\mathbf{b}_{\mathrm{a(t)}} + \mathbf{w}_{\mathrm{ab}}(\mathrm{t}) \\
[10pt]\dot{\mathbf{s}}_{\mathrm{g(t)}} = -\dfrac{1}{\mathrm{T}_{gs}}\mathbf{s}_{\mathrm{g(t)}} + \mathbf{w}_{\mathrm{gs}}(\mathrm{t}) \\
[10pt]\dot{\mathbf{s}}_{\mathrm{a(t)}} = -\dfrac{1}{\mathrm{T}_{\mathrm{ab}}}\mathbf{s}_{\mathrm{a(t)}} + \mathbf{w}_{\mathrm{ab}}(\mathrm{t})
\end{cases} \tag{4}$$

Compared to the continuous time differential equation (4), its discrete form is more commonly used in Kalman filtering:

$$\mathbf{x}_{\mathrm{k}} = \boldsymbol{\Phi}_{\mathrm{k/k-1}}\mathbf{x}_{\mathrm{k-1}} + \boldsymbol{\Gamma}_{\mathrm{k-1}}\mathbf{w}_{\mathrm{k-1}} \tag{5}$$

Equation (5) is referred to as the system state equation, where $\boldsymbol{\Phi}$ is the state transition matrix and $\mathbf{w}$ is the process noise of the discrete system. These are given as shown in Equation (6):

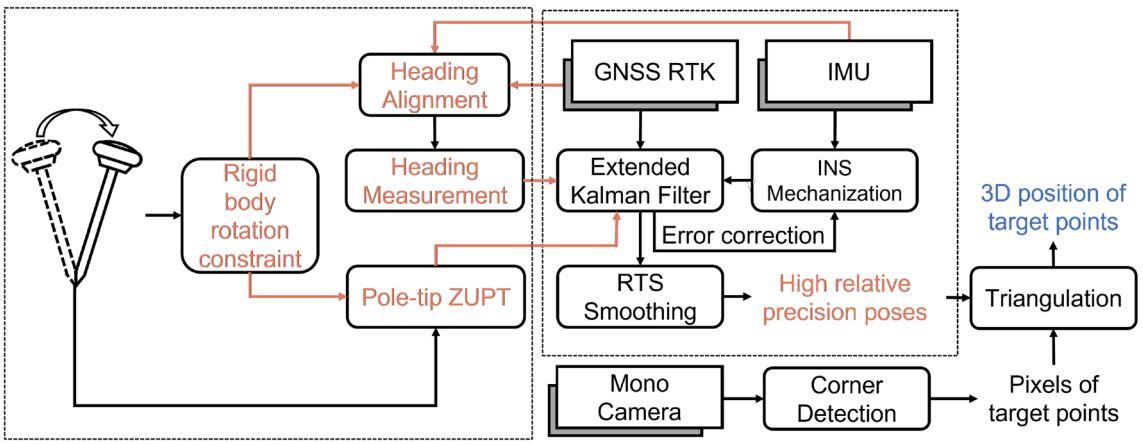

Fig. 4 Inertial photogrammetry RTK pole algorithm process

$$\begin{aligned}\mathbf{\Phi}_{k/k-1} &= \exp\left(\int_{t_{k-1}}^{t_k}\mathbf{F}(t)dt\right)\\ \mathbf{w}_{k-1} &= \int_{t_{k-1}}^{t_k}\mathbf{\Phi}_{k/t}\mathbf{G}(t)\mathbf{w}(t)dt\end{aligned} \tag{6}$$

Measurement model

The precision of the INS disperses over time, so external observations need to be introduced to maintain the pose precision. Typically, GNSS observations are used to perform absolute position corrections on the INS. However, relying solely on position corrections does not fully utilize the rigid body rotation motion characteristics of the surveying pole. In order to fully utilize this motion constraint, we introduced pole-tip zero velocity correction and heading correction to further suppress INS error divergence and provide higher-precision pose for subsequent photogrammetry.

Pole-tip zero velocity correction

When the surveying pole preforms the rigid body rotation motion, the pole-tip remains grounded and stationary. Therefore, the velocity at the pole-tip is nearly zero. The pole-tip zero velocity correction utilizes this motion characteristic to construct an observation equation. The observation vector is the difference between the pole-tip velocity estimated by INS and the actual pole-tip velocity, that is

$$\mathbf{z}_v = \hat{\mathbf{v}}_{tip}^n - \tilde{\mathbf{v}}_{tip}^n \tag{7}$$

Since the relation between the pole-tip velocity and the carrier velocity can be described as follows:

$$\begin{aligned}\mathbf{v}_{tip}^n =& \mathbf{v}_b^n + \mathbf{C}_b^n\left(\boldsymbol{\omega}_{eb}^b \times \mathbf{l}_{tip}^b\right) =\\ & \mathbf{v}_b^n - \left(\boldsymbol{\omega}_{ie}^n\times\right)\mathbf{C}_b^n\mathbf{l}_{tip}^b - \mathbf{C}_b^n\left(\mathbf{l}_{tip}^b\times\right)\boldsymbol{\omega}_{ib}^b\end{aligned} \tag{8}$$

Therefore, the pole-tip zero velocity measurement equation can be written in the following form:

$$\begin{aligned}\mathbf{z}_v =& \hat{\mathbf{v}}_{tip}^n - \tilde{\mathbf{v}}_{tip}^n = \hat{\mathbf{v}}_b^n -\\ & \left(\boldsymbol{\omega}_{in}^n\times\right)\left(\mathbf{C}_b^n\mathbf{l}_{tip}^b\times\right)\boldsymbol{\phi} - \left[\mathbf{C}_b^n\left(\mathbf{l}_{tip}^b\times\boldsymbol{\omega}_{ib}^b\right)\right]\times\boldsymbol{\phi}\\ & - \mathbf{C}_b^n\left(\mathbf{l}_{tip}^b\times\right)\delta\boldsymbol{\omega}_{ib}^b = \mathbf{H}_v\delta\mathbf{x} + \mathbf{n}_v\end{aligned} \tag{9}$$

Correspondingly, the design matrix $\mathbf{H}_v$ can be written as

$$\mathbf{H}_v = \left[0_3\ \mathbf{I}_3\ \mathbf{H}_{v3}\ -\left(\mathbf{C}_b^n\mathbf{l}_{tip}^b\times\right)\ 0_3\ \mathbf{H}_{v6}\ 0_3\right] \tag{10}$$

$\mathbf{H}_{v3}$ and $\mathbf{H}_{v6}$ are 3×3 matrices that are given by (11)

$$\begin{cases}\mathbf{H}_{v3} = -\left(\boldsymbol{\omega}_{in}^n\times\right)\left(\mathbf{C}_b^n\mathbf{l}_{tip}^b\times\right) - \left[\mathbf{C}_b^n\left(\mathbf{l}_{tip}^b\times\boldsymbol{\omega}_{ib}^b\right)\times\right]\\ \mathbf{H}_{v6} = -\mathbf{C}_b^n\left(\mathbf{l}_{tip}^b\times\right)\mathrm{diag}\left(\boldsymbol{\omega}_{ib}^b\right)\end{cases} \tag{11}$$

Heading correction

Chen et al. (2020)proposed a method for heading initialization by matching the trajectory derived from INS dead reckoning (DR) with the GNSS trajectory. The heading calculated through this method can also serve as a heading observation in the filtering process to correct the INS-derived results. The corresponding observation vector is the difference between the heading estimated by the INS and the heading calculated by this method.

$$\mathbf{z}_\psi = \hat{\boldsymbol{\psi}}_{nb} - \tilde{\boldsymbol{\psi}}_{nb} \tag{12}$$

The error differential equation of heading angle is as follows (Shin 2005)

$$\mathbf{H}_\psi = \left[0_3\ 0_3\ 0\ \mathbf{H}_{\phi 3}\ 0_3\ 0_3\ 0_3\ 0_3\ \right] \tag{13}$$

$\mathbf{H}_{\phi 3}$ can be expressed as

$$\mathbf{H}_{\phi 3} = \left[0\ \sec\theta\sin\phi\ \sec\theta\cos\phi\right] \tag{14}$$

Photogrammetric triangulization

For a certain target point P, its coordinates in the n-system are $\mathbf{r}_p^n$, and its pixel coordinates in the i-th frame are $\mathbf{p}_i$. According to the projection equation of the pinhole camera (Gao et al. 2017)

$$\lambda_i\mathbf{p}_i = \mathbf{K}\mathbf{C}_{n,i}^c\left(\mathbf{r}_p^n - \mathbf{r}_{c,i}^n\right) \tag{15}$$

where c is the camera coordinate system; $\mathbf{C}_n^c$ is the direction cosine matrix that projects the n-system vector to the c-system; $\mathbf{r}_c^n$ indicates the position of the camera in n-system; $\mathbf{K}$ is the camera intrinsic matrix; λ the pixel depth. $\mathbf{C}_n^c$, $\mathbf{r}_c^n$ are provided by INS

$$\begin{aligned}\left(\mathbf{C}_n^c\right)^T =& \mathbf{C}_c^n = \mathbf{C}_b^n\mathbf{C}_c^b\\ \mathbf{r}_c^n =& \mathbf{r}_b^n + \mathbf{C}_b^n\mathbf{l}_{bc}^b\end{aligned} \tag{16}$$

$\mathbf{C}_b^n$, $\mathbf{l}_{bc}^b$ are camera extrinsic parameters, which describe the relative relation between c-system and the b-system. There are now relatively mature algorithms for calibrating the camera extrinsic parameters(Rehder et al. 2016).

Rewrite (15) homogeneous form.

$$\lambda_i \mathbf{p}_i = \mathbf{K}\begin{bmatrix} \mathbf{C}^c_{n,i} & -\mathbf{C}^c_{n,i}\,\mathbf{r}^n_{c,i} \end{bmatrix}\begin{bmatrix} \mathbf{r}^n_p \\ 1 \end{bmatrix} \tag{17}$$

Since the vectors on both sides of the equation are collinear, hence (Hartley and Zisserman 2003)

$$p_i \times \mathbf{K}\begin{bmatrix} \mathbf{C}^c_{n,i} & -\mathbf{C}^c_{n,i}\,\mathbf{r}^n_{c,i} \end{bmatrix}\begin{bmatrix} \mathbf{r}^n_p \\ 1 \end{bmatrix} = 0 \tag{18}$$

Let $\mathbf{M}_i = \mathrm{p}_i \times \mathbf{K}\begin{bmatrix} \mathbf{C}^c_{n,i} & -\mathbf{C}^c_{n,i}\,\mathbf{r}^n_{c,i} \end{bmatrix}$ and establish the multi-frame equation

$$\begin{bmatrix} \mathbf{M}_1 \\ \mathbf{M}_2 \\ \mathbf{M}_3 \\ \cdots \end{bmatrix}\begin{bmatrix} \mathbf{r}^n_p \\ 1 \end{bmatrix} = \mathbf{A}\begin{bmatrix} \mathbf{r}^n_p \\ 1 \end{bmatrix} = 0 \tag{19}$$

The least square solution of $\mathbf{r}^n_p$ can be obtained by singular value decomposition (SVD) of $\mathbf{A}$.

Simulation experiment

The photogrammetric accuracy of the surveying pole is closely related to the camera pose precision and the geometry of the camera's observations. The higher camera pose precision and the better geometry, the higher photogrammetric accuracy. The shorter photogrammetric baseline and the farther target points from the camera, the worse geometry (Gao et al. 2017). Quantitative analysis and evaluation of the relation between these factors and surveying accuracy are essential for guiding algorithm design. However, due to the complex motion of the surveying pole, the numerous and coupled error sources in inertial navigation and photogrammetry, and the strong nonlinearity involved (Hong et al. 2005), it is generally not possible to derive the mathematical expressions and models for error propagation through analytical methods (Groves 2008). Carefully designed simulation experiments, which can closely approximate the field test results, have controllable error terms, and provide reference true values, are commonly used and almost the only feasible theoretical analysis method in this field (Weston and Titterton 2004; Groves 2008; Chen et al. 2021).

The overall flow of simulation data generation and result solving is shown in Fig. 5, which is divided into two major parts: the integrated navigation data simulation and the photogrammetric data simulation. Among them, the algorithm for integrated navigation data simulation is the most complex, as it requires both the simulated trajectory to exactly match the ideal simulated IMU and the simulated trajectory to closely resemble the actual IMU movement, especially simulating the rigid boy rotation motion of the surveying pole. To meet these requirements, we adopts a simulation method based on field test data of the surveying pole (Wang 2019; Li 2019; Hu 2020),which is done as follows: firstly, the GNSS/INS data collected by the surveying pole in the field test are solved by the integrated navigation algorithm, and the discrete position, speed and attitude sequences of the surveying pole are obtained. These serve as the input for inverse INS mechanization to obtain the ideal IMU output(Woodburn 2023). Then, IMU measurement errors are added to the ideal IMU output to obtain a simulated IMU (Hu et al. 2018). GNSS positioning errors are added to the reference position sequence to obtain the simulated RTK positioning results. Photogrammetric data simulation is relatively simpler. Its principle involves projecting the given coordinates of target points onto the camera plane to obtain pixel coordinates, based on the simulated reference position and attitude truth values (Hartley and Zisserman 2003).

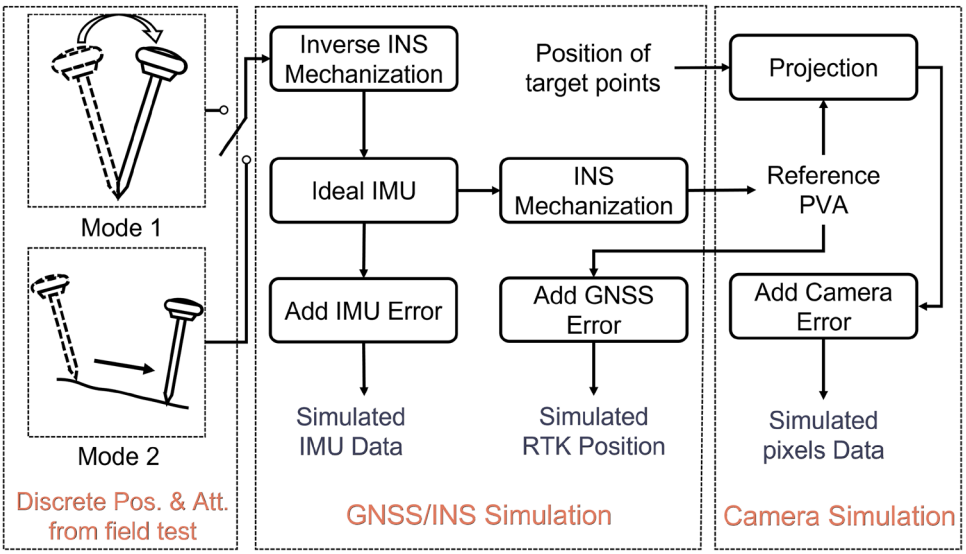

Fig. 5 Inertial Photogrammetry RTK Pole data simulation process

Table 1 Simulation experiment error parameters

Error source	Error model	Error parameters
RTK position error	GM1 & White noise	$T = 120\,s, \sigma = 0.003m$ $\boldsymbol{\omega} \sim \mathcal{N}(0, 0.002m)$
Gyro. ARW	Random Walk	$0.1deg/\sqrt{h}$
Accel. VRW	Random Walk	$0.1m/s/\sqrt{h}$
$\mathbf{g}_b$	GM1	$T = 3600s, \sigma = 50deg/h$
$\mathbf{a}_b$	GM1	$T = 3600s, \sigma = 50mGal$
$\mathbf{g}_s$	GM1	$T = 3600s, \sigma = 1000ppm$
$\mathbf{a}_s$	GM1	$T = 3600s, \sigma = 1000ppm$
pixel error	White noise	$\omega \sim \mathcal{N}(0, 1)$

Then, by incorporating random errors corresponding to the corner extraction accuracy observed in actual experiments (Garrido-Jurado et al. 2014), the simulated pixel coordinates of the target points are generated.

Relevant parameters of various error sources are shown in Table 1.

Considering that the GNSS RTK positioning error is not independent of each epoch, but related to the front and back epochs, the GNSS RTK positioning error is modeled as a first-order Gaussian Markov process (GM1), and white noise is added on this basis. The specific error parameters are obtained by Allan variance analysis(Niu et al. 2014). The inertial navigation error parameter is the optimization result of adis16465 in the actual integrated navigation solution(Zhang 2015; El-Sheimy and Youssef 2020). The pixel error is modeled as white noise, and the error comes from the empirical value of corner extraction accuracy in the actual experiment(Garrido-Jurado et al. 2014).

Pose precision verification

Most of the visual RTK products on the market are used by holding the pole walking for a certain distance (e.g. 4–8 m), observing the target points from different perspectives during the walk. This method allows for a longer photogrammetric baseline (walking distance) and better photogrammetric geometry. In contrast, the method proposed in this paper, where the surveying pole is swung to observe the target points, results in a limited baseline length during the photogrammetry process, typically ranging from 1.5 to 2 m. Under these conditions, to achieve the same photogrammetric accuracy as the walking mode, the inertial navigation system must provide higher position and attitude precision to the camera. This paper improves the position and attitude precision by fully utilizing the rigid body rotation characteristics of the surveying pole and introducing velocity and heading constraints.

In order to verify the feasibility of swinging the surveying pole at a fixed point to provide high-precision pose, three groups of simulation experiments are designed in this paper:

(1) Swinging the surveying pole at a fixed point (the baseline length is 1.5–2 m), using rigid body rotation constraints(RBRC) in the data processing;
(2) Swinging without using RBRC in the data processing;
(3) Walking a certain distance while holding the pole

Since photogrammetric accuracy is highly correlated with the relative pose (position and attitude) precision between camera epochs, while the absolute camera pose accuracy has less effect on photogrammetric accuracy, this paper focuses on the pose precision between epochs. The pose precision is defined as follows:

$$\begin{aligned} \Delta\delta\mathbf{r}^{n}_{b_{t,t-\Delta t}} &= ||\delta\mathbf{r}^{n}_{b_t} - \delta\mathbf{r}^{n}_{b_{t-\Delta t}}|| \\ \Delta\delta\boldsymbol{\phi}_{t,t-\Delta t} &= ||\boldsymbol{\phi}\left(\mathbf{C}^{b_t}_{b_{t-\Delta t}}\left(\hat{\mathbf{C}}^{b_t}_{b_{t-\Delta t}}\right)^{-1}\right)|| \end{aligned} \tag{20}$$

From Eq. (20), it is clear that the time interval between epochs also affects the calculation of pose precision. Considering that one complete swing of the surveying pole typically takes around 5 s, the value of Δt is taken as 5 s.The relative pose precision for the three sets of experiments defined in equation (20) is shown in Fig. 6. It can be observed that the two motion modes - swinging and walking - have a negligible effect on the INS pose precision. However, the rigid body rotation constraint significantly improves the position precision, which in turn contributes to enhancing the accuracy of short-baseline high-precision photogrammetry.

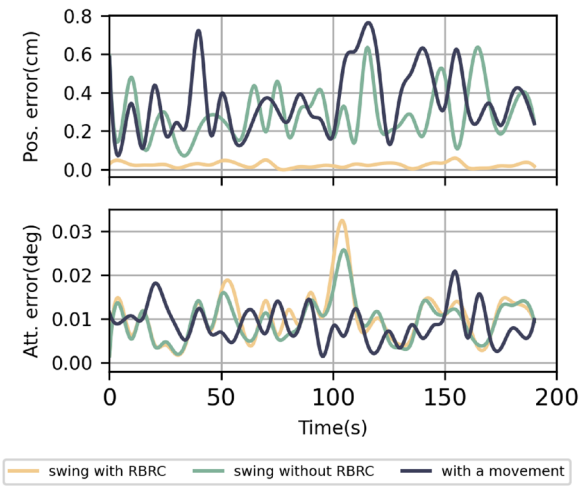

Fig. 6 Comparison of position(pos.) and attitude(att.) precision among three experiments

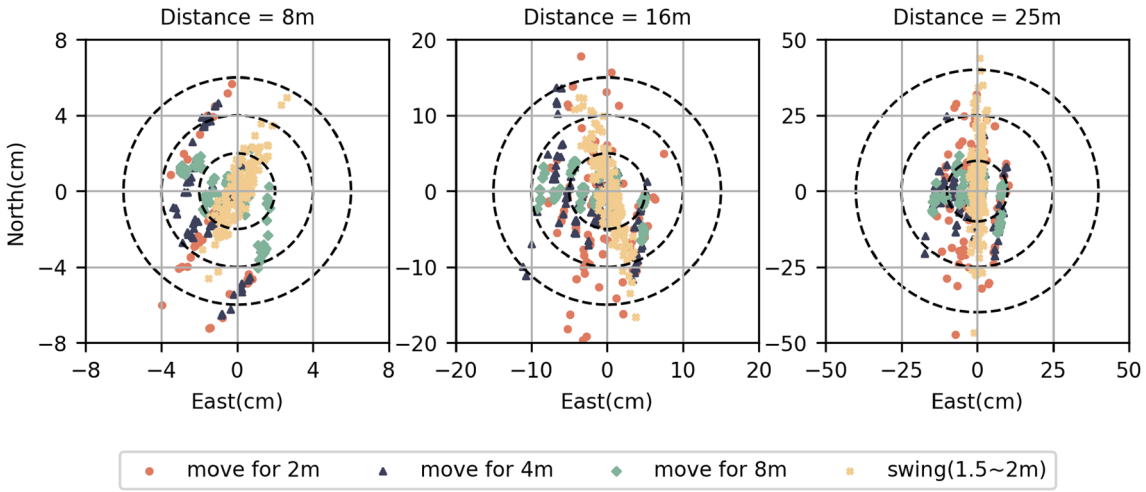

Fig. 7 The error scatter plots of target points with different distances and with different baseline lengths, in the simulation. (The simulation walking/swing trajectory input is from the field test data, and the camera observes toward north direction during the field test)

Photogrammetry accuracy verification

This section tests and evaluates the photogrammetric precision of the target points in the two modes of waving and walking. For this purpose, a simulation experiment is designed as shown in the Table 2

The length of the photogrammetric baseline determines the quality of the photogrammetric geometry observation conditions and is highly correlated with photogrammetric accuracy. The simulation experiments designed the photogrammetry with swinging the surveying pole at a fixed point (1.5–2 m baseline) and three different baseline lengths for handheld walking mode (2 m, 4 m, and 8 m) to assess the relation between baseline length and photogrammetric accuracy. The 2 m baseline serves as the control experiment for the swing experiment, while the 4 m and 8 m baselines are typical baseline lengths for visual RTK to complete a photogrammetry task. on the one hand, this setup allows for a quantitative evaluation of the relation between photogrammetric accuracy and baseline length for handheld walking, and on the other hand, it helps assess the accuracy achievable by the swinging compared to walking a certain distance.

The photogrammetric accuracy for the four sets of simulation experiments is shown in Fig. 8. In the figure, the scatter points correspond to each targets points' distance from the camera and its surveying accuracy, while the curve is the result of curve fitting based on the scatter points, reflecting the trend of surveying accuracy with varying observation distances. From the figure, it can be observed that, with roughly the same baseline length, the photogrammetric accuracy achieved by swinging is significantly higher than that of the handheld walking method. Within a 15 m distance, swinging the surveying pole at a fixed point has a considerable advantage due to the high pose precision it provides to the camera. The surveying accuracy remains within 6 cm, which is better than the handheld walking method at a 4 m baseline. However, as the distance increases, the disadvantage of the short photogrammetric baseline of the swinging mode becomes apparent, and the error exceeds that of the

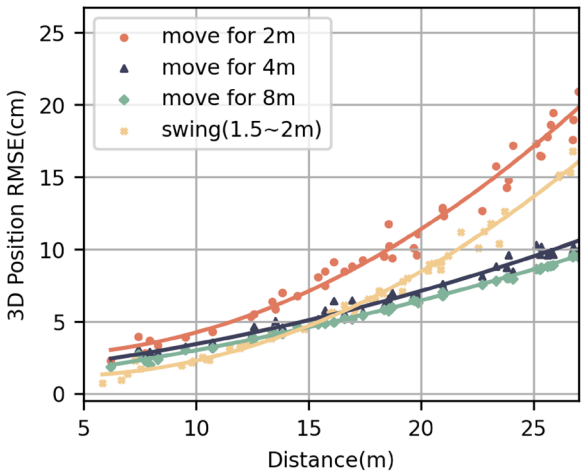

Fig. 8 The root mean squared error (RMSE) of the target points varies with the observation distance and the baseline lengths

Table 2 Design of photogrammetry simulation experiment

Motion type	Number of target points	Image frequence (Hz)	Independent simulations
swing (1.5–2 m)	50	5	100
move for 2 m	50	5	100
move for 4 m	50	5	100
move for 8 m	50	5	100

handheld walking at a 4 m baseline. The handheld walking at an 8 m baseline can consistently maintain high photogrammetric accuracy, with a RMSE of approximately 10 cm at a 25 m distance. Fig. 7 shows the plane error distribution of the target points for three typical surveying distances of 8 m, 15 m and 25 m. It can be seen that the position error under the condition of swinging the pole is mainly concentrated in the north–south direction. This is because, in the simulation experiment, the camera observes the target points from south to north, so the north–south direction is the depth direction. Because the baseline of swinging is short, the geometry observation conditions are poor, and there is great uncertainty in the depth estimation, there is a large error in the north–south direction. However, the problem does not exist for the 4/8 m handheld walking due to the better geometric observation conditions, and the error is evenly distributed in the north–south and east–west directions.

It is worth noting that in Fig. 8, the surveying errors of the points do not strictly increase with the observation distance but rather fluctuate around the curve. This is partly because the simulation pixel error is random, and partly because the camera's observation azimuth also affects the photogrammetric geometry. As shown in Fig. 9, three target points (yellow circles) are distributed on a dashed circle centered on the camera's position (green circle), all at the same distance from the camera. When the camera moves in the east–west direction (blue wavy line) and observes these three points to the north, the photogrammetric geometry and surveying accuracy change due to different observation azimuth angles (θ).As the observation azimuth increases, the geometry becomes worse, and the measurement accuracy decreases accordingly.

In order to quantitatively evaluate this effect, a number of target points with the observation angle varying from –30° to 30° at a distance of 15 m are generated by using the simulation program. When the surveying pole swinging, the accuracy and observation azimuth angle of the target points are shown in the Fig. 10

It can be seen that when the observation angle changes from 0 to 30°, the measurement accuracy in the horizontal

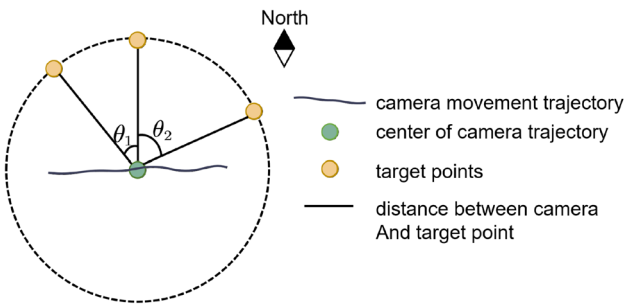

Fig. 9 Schematic diagram of camera observation angle

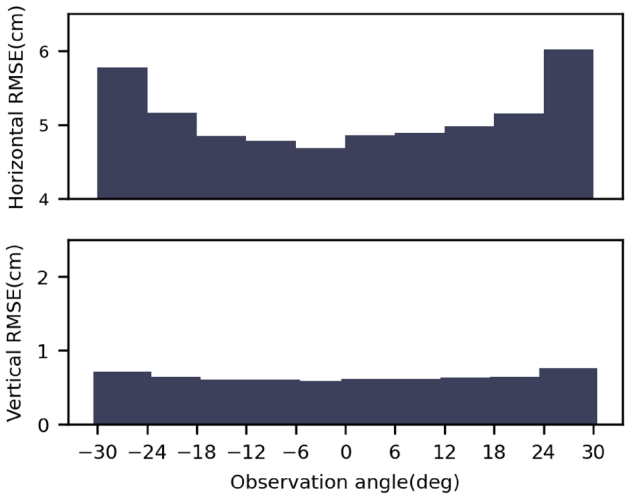

Fig. 10 The relation between observation angle and accuracy of the target points (distance=15 m)

direction decreases by about 1 cm, while the measurement accuracy in the vertical direction changes very little.This is because, as the observation angle changes, the photogrammetric geometry in the horizontal direction deteriorates, whereas the vertical direction remains unaffected. Therefore, when there are high requirements for observation accuracy, the motion trajectory of the surveying pole should be adjusted to keep it perpendicular to the observation direction of the camera.

Field test

Field tests were carried out to validate the surveying accuracy of the inertial photogrammetry RTK pole. As shown in Fig. 11, the experiment was conducted in an open area with good GNSS visibility. The PDOP (Position Dilution

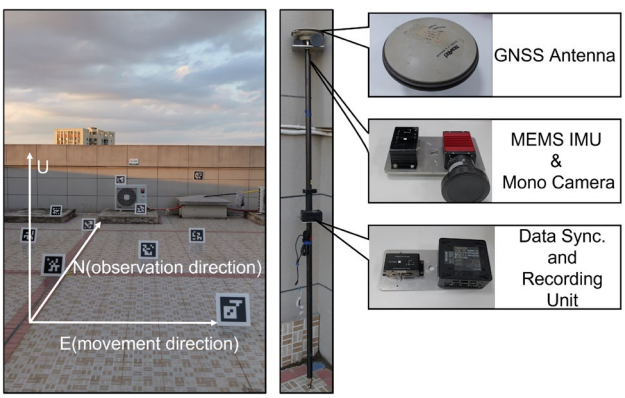

Fig. 11 Experiment field and data acquisition equipment

of Precision) and observation precision are presented in Fig. 12. In this test area, QR code boards were placed from south to north at distances ranging from 5 to 17 m from the camera, and the corners of these QR boards were used as photogrammetry target points. Their reference coordinates were obtained using a high-precision total station, with an error margin of less than 1 cm. During the experiment, the surveying pole was initially swung at fixed point in an open area for initialization. Then, the pole was moved in an east–west direction (by swinging at a fixed point or walking while holding the pole) to observe the QR code boards arranged in the north–south direction. Throughout the movement, the camera's orientation needed to be constantly adjusted to ensure all target points were observed.

The surveying pole used for data collection is shown in Fig.11. From top to bottom, it is equipped with a GNSS antenna, a camera-IMU platform, a data synchronization and recording unit. The extrinsic parameters between the camera and IMU was determined using an existing calibration algorithm(Rehder et al. 2016). The specific sensor models mounted on the surveying pole are listed in Table 3.

Pose precision verification

Firstly we designed a field test to validate the pose precision of the inertial photogrammetry RTK pole. Due to the large movement amplitude of the pole and its limited load capacity, it is challenging to directly obtain reference truth values by mounting high-precision inertial navigation devices. Therefore, this study indirectly analyzes the pose precision by evaluating the projection error of target points: when the reference truth values of the target points are known, they can be projected onto the image plane based on the pinhole camera projection (21).

$$\hat{\mathbf{p}}\left(\hat{\mathbf{C}}_{\mathrm{n}}^{\mathrm{c}}, \hat{\mathbf{r}}_{\mathrm{p}}^{\mathrm{n}}\right) = \frac{\mathbf{K}\hat{\mathbf{C}}_{\mathrm{n}}^{\mathrm{c}}\left(\hat{\mathbf{r}}_{\mathrm{p}}^{\mathrm{n}} - \mathbf{r}_{\mathrm{c}}^{\mathrm{n}}\right)}{\lambda} \tag{21}$$

Then, the difference between $\hat{\mathbf{p}}$ and the pixel coordinates of the target points extracted from the photos($\tilde{\mathbf{p}}$) is the projection error

Table 3 Equipment description for Inertial Photogrammetry RTK Pole

Sensors	Description
GNSS antenna	NovAtel GPS-7-2GGL
IMU	MEMS IMU, ADIS16465-2, sampling rate 200Hz
Camera	Prosilica GT1910, Sampling rate 5Hz Resolution 1920 x 1080, pixel size 5.5 microns
Surveying pole	Trimble Surveying Pole, 2 m in length

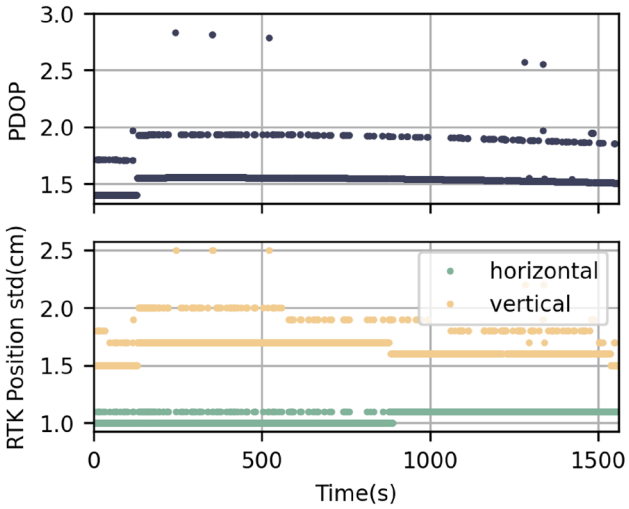

Fig. 12 PDOP and RTK observation precision

$$\mathbf{e} = \tilde{\mathbf{p}} - \hat{\mathbf{p}}\left(\hat{\mathbf{C}}_{\mathrm{n}}^{\mathrm{c}}, \hat{\mathbf{r}}_{\mathrm{p}}^{\mathrm{n}}\right) \tag{22}$$

To compare the pose precision of the surveying pole under two motion modes: swinging and walking, the study conducted approximately 4 min of observation for a single QR code target point using both motion forms. It is important to note that 4 min is significantly longer than the time required to complete a single photogrammetry measurement; this extended duration was used solely to validate the pose precision of the surveying pole. To prevent large changes in the azimuth of the camera's observations during handheld walking, the experiment involved walking back and forth within an 8 m range rather than moving continuously in a fixed direction. As shown in Fig. 13, the projection errors for the two motion modes indicate that in the case of swinging

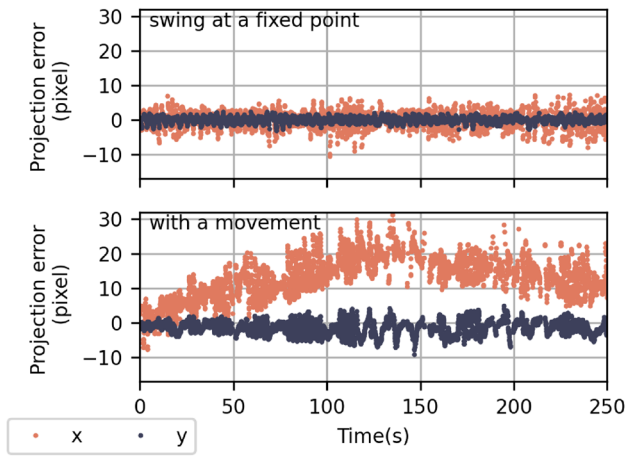

Fig. 13 Photogrammetry projection error of two motion modes (distance=15 m)

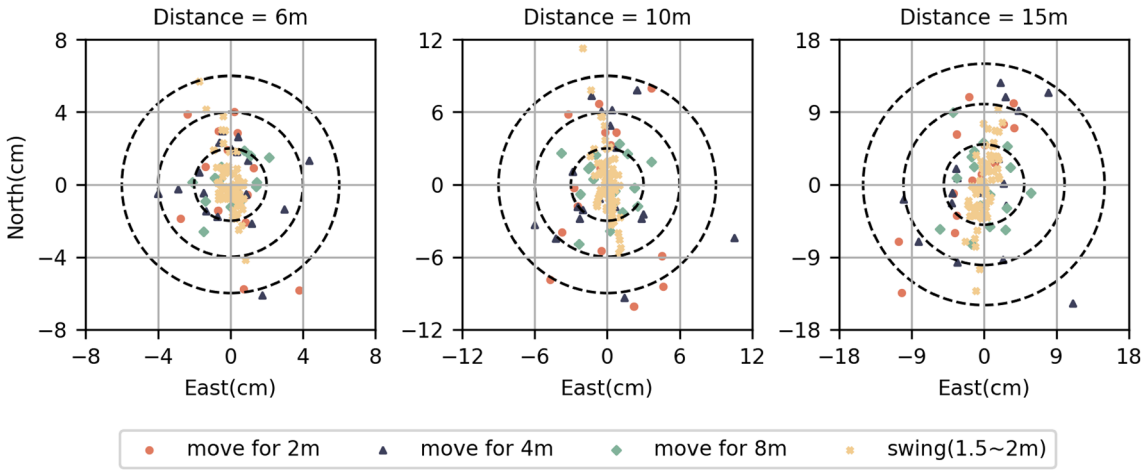

Fig. 14 The error scatter plots of target points with different distances and with different baseline lengths, in the field tests

Table 4 Experiment design for field test

Motion type	Duration(s)	Image count	Independent repetitions
swing(1.5–2 m)	10	50	70
move for 2 m	15	75	20
move for 4 m	30	150	20
move for 8 m	60	300	20

at a fixed point, the projection errors in the x and y directions are relatively small and fluctuate steadily around the horizontal axis. In contrast, when handheld walking, the y-axis projection error exhibits systematic drift, suggesting that the horizontal position or heading precision of the pole is lower in this mode. This demonstrates that the pose precision is higher when swinging, confirming that swinging at a fixed point is a feasible method for achieving high-precision photogrammetry with a short baseline.

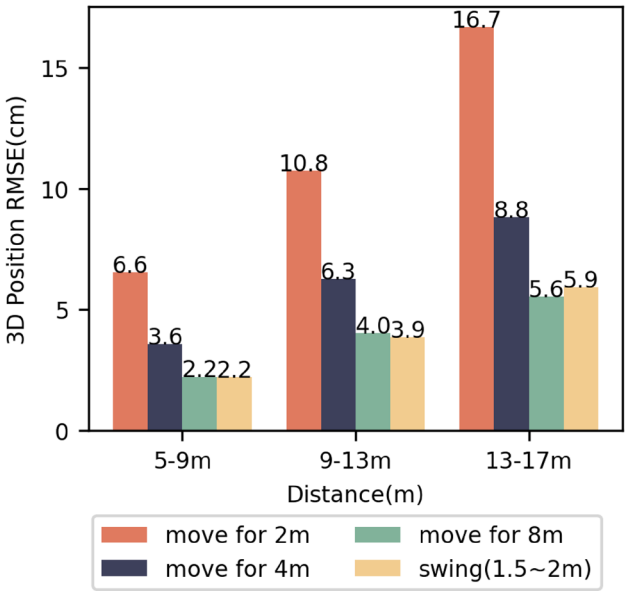

Fig. 15 RMSE of target points with different distances and with different baseline lengths

Photogrammetry accuracy verification

To evaluate the photogrammetry accuracy of the two modes, the experiment outlined in Table 4 was designed. During the handheld walking mode, it was necessary to continuously adjust the camera's heading to ensure all target points were observed, which resulted in a slower walking speed than a typical walking pace.

There were 12 QR code boards in the field, categorized into three groups based on their distance from the camera: 5–9 m, 9–13 m, and 13–17 m. The photogrammetry accuracy for the target points within each distance range was analyzed, with results shown in Fig. 15.

Overall, the field experiment demonstrated that the surveying accuracy of the target points and its variation with observation distance/baseline length aligns with the trends observed in the simulation experiments. Surveying accuracy decreased as the distance from the camera increased. In the handheld walking mode, accuracy improved as the walking distance increased. Walking 4 m ensures surveying accuracy within approximately 6 cm for target points up to 13 m away, while walking 8 m achieves a similar accuracy for points up to 17 m away.

As shown in Fig. 14, within a 15 m range, the advantage of high pose accuracy in the swinging mode becomes apparent. The geometry advantage of handheld walking 8 m is

less pronounced. Both swinging and walking modes achieve similar photogrammetry accuracy, with RMSE of approximately 6 cm. At the 15 m distance, although the swinging mode shows a larger error in the depth (north–south) direction than the 8 m walking mode, its error distribution is more concentrated in the east–west direction. This indicates that the swinging mode has higher precision in terms of heading/horizontal positioning.

The above experiments demonstrate that the swinging at a fixed point can achieve a surveying accuracy approximately 4 cm at a 10 m distance and 6 cm at a 15 m distance, comparable to the accuracy achieved by handheld walking 8 m. This makes swinging mode a time- and effort-efficient measurement method.

Conclusion

To solve the issues of current visual RTK, including limited application scenarios, tedious operation process, unreliable and inconsistent accuracy, this paper proposes a new method that achieves high-precision RTK photogrammetic point surveying by swinging the surveying pole with the pole tip contact at a fixed point (instead of holding the pole and walking). Relevant algorithm is designed and validated by simulation and field test results. A detailed accuracy analysis of the proposed swinging method and the existing handheld walking method are made in a comparison way.

The swinging mode makes full use of the fix-point rotation of rigid body to provide the camera with a high-precision pose and then realize high-precision photogrammetry. The surveying accuracy of the swinging mode (with 1.5–2 m baseline) beat the handheld walking mode with 8 m baseline, for the target points within 15 m, achieving approximately 6 cm RMSE at 15 m, 4 cm RMSE at 10 m, and 2 cm RMSE at 6 m.

Acknowledgements The authors would like to thank Dr. Tisheng Zhang and Dr. Hailiang Tang in our group for providing the INS-Probe in the field test, and thank Changxin, Lai for his help in the experiment, and thank Xuanyou, Chen for his help in the experiment.

Funding This work was supported in part by the National Natural Science Foundation of China under Grant 42374028, as well as by the LIESMARS Special Research Funding and the open project fund of the National Engineering Research Center for Digital Construction and Evaluation Technology of Urban Rail Transit, China.

Data availability The datasets are available from the corresponding author.

Declarations

Conflict of interest The authors declare that they have no Conflict of interest.

References

Bruno MS (2009) AINS enhanced survey instrument. Patent No. US20090024325A1. US Patent

Chen Q, Lin H, Guo R, Niu X (2020) Rapid and accurate initial alignment of the low-cost mems imu chip dedicated for tilted rtk receiver. GPS Solut 24(4):119. https://doi.org/10.1007/s10291-020-01032-8

Chen Q, Zhang Q, Niu X, Liu J (2021) Semi-analytical assessment of the relative accuracy of the gnss/ins in railway track irregularity measurements. Satell Navig 2:1–16

Colomina I, Molina P (2014) Unmanned aerial systems for photogrammetry and remote sensing: A review. ISPRS J Photogramm Remote Sens 92:79–97

Deng L, Guo J, Ma J, Zhao Y, Xu Y (2022) Gnss rtk positioning and accuracy analysis for the oblique compensation technology. GEOSPATIAL INFORMATION

El-Sheimy N, Youssef A (2020) Inertial sensors technologies for navigation applications: state of the art and future trends. Satell Navig 1(1):2

Gao X, Zhang T, Liu Y, Yan Q (2017) 14 Lectures on Visual SLAM: From Theory to Practice. Publishing House of Electronics Industry, China

Garrido-Jurado S, Muñoz-Salinas R, Madrid-Cuevas FJ, Marín-Jiménez MJ (2014) Automatic generation and detection of highly reliable fiducial markers under occlusion. Pattern Recogn 47(6):2280–2292. https://doi.org/10.1016/j.patcog.2014.01.005

Groves PD (2008) Principles of GNSS, Inertial, and Multisensor Integrated Navigation Systems. Artech House, Boston

Guo R (2021) Research on point measurement algorithm of hand-held mobile measuring pole. Master's thesis, Wuhan University

Guo R, Jiang J, Niu X, Shi J (2020) Monocular vision coordinate transfer method with imu aiding. Bull Surv Map 3:7–11

Gučević J, Delčev S, Vasović Šimšić O (2024) Practical limitations of using the tilt compensation function of the gnss/imu receiver. Remote Sens. https://doi.org/10.3390/rs16081327

Hartley R, Zisserman A (2003) Multiple View Geometry in Computer Vision. Cambridge University Press, Cambridge

Hong S, Lee MH, Chun H-H, Kwon S-H, Speyer JL (2005) Observability of error states in gps/ins integration. IEEE Trans Veh Technol 54(2):731–743

Hu Y (2020) Fast evaluation scheme for mems imu navigation performance based on emulation method. Master's thesis, Wuhan University

Hu Y, Zhang Q, Niu X (2018) Effects of IMU bias correlation time on GNSS / INS integrated navigation results based on the first order gauss-Markov model. Sci Technol Eng 18(34):236–241

Knut S (2020) Surveying system. Patent No. US10495461B2. US Patent

Lai C (2022) Research on position measuring technique using a low-cost inertial-aided positioning pole in GNSS-denied environment. Master's thesis, Wuhan University

Lai C, Guo R, Chen Q, Niu X (2023) Extending the real-time kinematics survey method to global navigation satellite system-denied areas using a low-cost inertial-aided positioning pole. NAVIGATION: Journal of the Institute of Navigation. 70(3)

Li K, Chen Y (2019) Analysis of High Precision RTK Tilt Measurement Technologies. In: The 10th China Satellite Navigation Conference

Li Y (2019) Research on technique foot-mounted imu based pedestrian navigation. Master's thesis, Wuhan University

Lin H (2021) High-precision rtk positioning with tilt compensation: Data fusion algorithm. In: Proceedings of the 34th International Technical Meeting of the Satellite Division of The Institute of Navigation (ION GNSS+ 2021), pp. 2681–2695

Liu J, Gao K, Guo W, Cui J, Guo C (2020) Role, path, and vision of "5g+ bds/gnss''. Satell Navig 1(1):23

Luo X, Schaufler S, Carrera M, Celebi I (2018) High-precision rtk positioning with calibration-free tilt compensation. In: Proceedings of the FIG Congress

Mark E, N, Nicholas CT (1996) Pole-tilt sensor for surveyor range pole. Patent No. US5512905A. US Patent

Niu X, Chen Q, Zhang Q, Zhang H, Niu J, Chen K, Shi C, Liu J (2014) Using allan variance to analyze the error characteristics of gnss positioning. GPS Solut 18(2):231–242. https://doi.org/10.1007/s10291-013-0324-x

Peppa MV, Morelli L, Remondino F, Mills JP (2024) 3d geometric assessment of a commercial rtk/ppp visual positioning mobile sensor. Int Arch Photogramm Remote Sens Spat Inf Sci 48:97–104

Rehder J, Nikolic J, Schneider T, Hinzmann T, Siegwart R(2016) Extending kalibr: Calibrating the extrinsics of multiple imus and of individual axes. In: 2016 IEEE International Conference on Robotics and Automation (ICRA)

Schaufler S, Fischell M, Boffi G, Luo X, Török Z (2020) An innovative image-based surveying approach for globally referenced remote point measurements. In: Proceedings FIG Congress

Shin E-H (2005) Estimation techniques for low-cost inertial navigation. PhD thesis, University of Calgary, Deparment of Geomatics Engineering

Štroner M, Urban R, Reindl T, Seidl J, Brouček J (2020) Evaluation of the georeferencing accuracy of a photogrammetric model using a quadrocopter with onboard gnss rtk. Sensors 20(8):2318

Štroner M, Urban R, Seidl J, Reindl T, Brouček J (2021) Photogrammetry using uav-mounted GNSS RTK: Georeferencing strategies without GCPS. Remote Sens 13(7):1336

Teunissen P, Montenbruck O (2017) Springer Handbook of Global Navigation Satellite Systems. Springer, Switzerland

Wang Q (2019) Research on simulation technique of integrated navigation based on ins mechanization. Master's thesis, Wuhan University

Wang X, Yang Z, Chen K, Sun F, Li X (2025) A gnss/ins tilt measurement method considering lever arm error. J Chin Inert Technol 33(03), 219–228 . https://doi.org/10.13695/j.cnki.12-1222/o3.2025.03.002

Weston JL, Titterton DH (2004) Strapdown inertial navigation technology. Institution of Electrical Engineers and American Institute of Aeronautics and Astronautics

Woodburn D (2023) Tutorial on inverse mechanization. In: Proceedings of the 36th International Technical Meeting of the Satellite Division of The Institute of Navigation (ION GNSS+ 2023), pp. 23–37

Wu C, Chen Y, Li C, Pan G (2024) A non-contact tilt compensation method based on monocular camera/gnss/ins. In: Yang C, Xie J (eds) China Satellite Navigation Conference (CSNC 2024) Proceedings. Springer, Singapore

Zhang Q (2015) Research on analysis methodology and applications of short-term accuracy of gnss/ins integration. PhD thesis, Wuhan University

Publisher's Note Springer Nature remains neutral with regard to jurisdictional claims in published maps and institutional affiliations.

Springer Nature or its licensor (e.g. a society or other partner) holds exclusive rights to this article under a publishing agreement with the author(s) or other rightsholder(s); author self-archiving of the accepted manuscript version of this article is solely governed by the terms of such publishing agreement and applicable law.